Nanoscale

PAPER

Cite this: *Nanoscale*, 2025, **17**, 25239

Engineering ultra-small nanoceria with antioxidant and UV-shielding properties as functional nanomaterials in composite coatings for complex surface protection

Erica Galvagno,[a,b] Sergio Marras,[c] Silvia Dante,[c] Rosaria Brescia,[d] Miquel Gamón Rodríguez,[e] Alessio Carmignani,[f] Matteo Battaglini,[f] Gianni Ciofani,[f] Raffaella Lamuraglia,[a] Federica Menegazzo,[b] Arianna Traviglia *[a] and Mauro Moglianetti *[a]

Received 24th June 2025,
Accepted 18th September 2025

DOI: 10.1039/d5nr02680f

rsc.li/nanoscale

The development of advanced catalytic shields against UV-induced and oxidative degradation phenomena is critical to address multifaceted deterioration processes. The maximization of the surface-to-volume ratio in ultra-small cerium oxide nanoparticles (CeO_2 NPs) favors the Ce(III)/Ce(IV) exchange on the surface and the formation of oxygen vacancies, creating an ideal platform to target entangled degradation issues. Here, we design a microwave-assisted scalable process to obtain highly stable CeO_2 NPs (2 nm), and we demonstrate the redox cycling of the nanocatalyst by means of environmental XPS. Thereafter, we develop a polymer nanocomposite formulation in which the biopolymer and the catalytic nanomaterial work synergistically to provide a protective action without hindering the active sites present at the surface of the NPs. We test the protective action of the coating in the challenging context of cultural heritage, investigating its performance on ancient frescoes. Their surfaces are often subjected to pigment degradation, triggered by a combination of light, salts, and high relative humidity. We verify how, thanks to the joint action of the biopolymer and the NPs, the CeO_2 NP-based coating effectively mitigates complex deterioration mechanisms.

Introduction

Functional nanomaterials represent a highly promising domain for creating advanced catalytic shields capable of mitigating complex deterioration pathways triggered by UV exposure and oxidative species. Cerium oxide nanoparticles (CeO_2 NPs) emerge as ideal candidates to simultaneously overcome both challenges, owing to their dual antioxidant and UV-shielding functionalities. Their versatility arises from the formation of oxygen vacancies and the efficient Ce(III)/Ce(IV) redox cycling at the surface.[1–5] However, despite their great potential, their application as functional components of protective coatings remains limited, especially in the protection of painted surfaces and cementitious structures.[5–8] To date, scientific efforts have predominantly focused on using CeO_2 NPs in coatings designed for metal corrosion protection, while UV-shielding and anti-ageing coatings have only been marginally explored.[8–12] Furthermore, their UV-shielding properties have been used to slow down the ageing process of polymeric matrixes, overlooking their potential in the protection of the underlying substrate.[9,13] Several limitations have emerged in recent coating applications and novel strategies are needed to overcome them. First, it is crucial to rigorously define the function of the NPs within complex multicomponent systems. Indeed, an insufficient evaluation can compromise the design of accurately engineered strategies.[9–11,13,14] Additionally, investigations should aim at optimized integration of the NPs into polymeric and epoxydic matrixes. The focus on this key point allows to overcome issues related to aggregation phenomena, which can severely diminish catalytic efficiency and reduce optical transparency.[13,15,16]

To address these issues, it is important to enhance the efficiency of the NPs and preserve their protective function

---

[a] *Center for Cultural Heritage Technology (CCHT), Istituto Italiano di Tecnologia (IIT), Via A. Olivetti 1, Roncade, TV, 31056, Italy. E-mail: mauro.moglianetti@iit.it, arianna.traviglia@iit.it*

[b] *Department of Molecular Sciences and Nanosystems, Università Ca' Foscari Venezia, Via Torino 155, Venezia Mestre, 30172, Italy*

[c] *Materials Characterization Facility, Istituto Italiano di Tecnologia (IIT), Via Morego 30, 16163 Genova, Italy*

[d] *Electron Microscopy Facility, Istituto Italiano di Tecnologia (IIT), Via Morego 30, 16163 Genova, Italy*

[e] *Department of Surface and Plasma Science, Faculty of Mathematics and Physics, Charles University, V Holešovičkách 2, 180 00 Praha 8, Czech Republic*

[f] *Smart Bio-Interfaces, Istituto Italiano di Tecnologia (IIT), 56025 Pontedera, Italy*

within the polymeric matrix.[17] First, by producing ultra-small stable NPs, superior performances can be accomplished thanks to the increase in the surface-to-volume ratio.[18–21] Studies in the literature on 3 nm CeO_2 NPs highlight challenges in achieving sufficient stabilization in solution, leading to partial aggregation and, hence, loss of function.[22–25] It is fundamental to overcome this issue and define how the ultra-small size can influence the catalytic activity of the NPs compared to the larger NPs reported in the majority of studies.[26–28] Moreover, the design of the polymer nanocomposite has to be accurately engineered to ensure a strong synergistic interaction between the NPs and the polymeric matrix. Due to their combined action, the coating can reliably perform even under the most challenging conditions. To provide incontrovertible proof of this premise, we sought to identify the most complex type of surface to test the coating's ability to prevent irreversible changes. The field of cultural heritage conservation responds to this need and ancient frescoes constitute a solid case study to test degradation in outdoor environments. In this specific context, darkening processes have been observed for several pigments, with cinnabar being an emblematic example.[29–34] Given the system's complexity, current conservation strategies have proven insufficient in effectively mitigating pigment degradation. Instead, the field predominantly relies on the use of synthetic polymers or resins.[35–40] Additionally, in the last two decades, NPs with specific functions have emerged as promising strategies, but none of them appears to have the required properties to tackle the issue of color change in frescoes, which often involves both UV-induced phenomena and redox mechanisms.[41–53] The strict requirements of the field add a degree of complexity to the formulation of innovative protective strategies. Indeed, artworks require far more sophisticated conservation approaches than any contemporary material. In particular, the field of cultural heritage conservation demands a precise set of characteristics for any protective product. To this aim, the coating should present a delicate combination of transparency, water vapor permeability, long-lasting efficacy, and efficient barrier effect.[35,54,55]

In this work, we have produced ultra-small CeO_2 NPs aiming at maximizing the surface-to-volume ratio and, simultaneously, improving the catalytic performances by favoring the Ce(III)/Ce(IV) conversion at the surface. We have established a well-defined structure–function relationship and ascertained the response of the NPs to the interaction with different environmental factors (*i.e.*, light, oxygen-based species, and high temperature). Furthermore, we have developed a chitosan formulation to evenly distribute the NPs on the substrates and provide extensive protection thanks to its barrier effect and filming properties.[56] Lastly, we tested the coating against the degradation of cinnabar (HgS) in frescoes, a critical process caused by the simultaneous presence of light, salts, and high relative humidity. We demonstrated that the synergy between the polymeric matrix and the catalytic properties of the NPs slows down or even halts the deterioration of cinnabar, paving the way to its cross-field application.

Results and discussion

Synthesis and characterization of CeO_2 NPs

The development of nanomaterials with enhanced catalytic activity is a critical step to produce efficient, effective, and sustainable systems with optimal performances. To achieve this task, we focused on strategies to maximize the surface-to-volume ratio with the final aim of increasing the number of available active sites on the surface per given mass of NPs. Indeed, size is a decisive factor as it affects the extent of surface that is available for the catalytic activity. For this reason, we designed and scaled up a synthetic protocol to produce ultra-small CeO_2 NPs, leveraging on a recently published hydrothermal protocol.[57] The synthesis was performed in an aqueous environment and the NPs were stabilized with sodium citrate. This capping agent improves the stability of the NPs in the dispersion by avoiding aggregation phenomena. Contrarily to the published synthesis, we implemented a microwave-assisted protocol and tested both tetramethylammonium hydroxide, TMAOH, and ammonium hydroxide, NH_4OH, to create the required alkaline environment. In this section, we compared the characteristics of the resulting NPs, named t-NPs and a-NPs, respectively.

The XRD pattern of the a-NPs is in agreement with the expected fluorite structure (space group *Fm*3*m*(225)), confirming the formation of crystalline cubic CeO_2 NPs (Fig. 1a). Size analysis from XRD data establishes that the average diameter of the NPs in powder form is equal to 3.18 ± 0.06 nm. These data are representative of the whole sample, but they could be affected by aggregation phenomena established during the freeze-drying process implemented to obtain the NPs powder. Therefore, TEM and SAXS analyses were also performed, and they prove that ultra-small citrate-capped NPs were synthesized. From the analysis of the TEM images presented in Fig. 1b and S1a, an average diameter of 2.2 ± 0.4 nm was calculated for the a-NPs. The t-NPs present a similar size distribution centered at 2.1 ± 0.4 nm (Fig. S1b). In both cases, the size is homogeneous throughout the portion of NPs analyzed, and the NPs are well separated despite the potential influence of solvent evaporation on their aggregation. We achieved a polydispersity of about 18.2%; this result is in line with recently published reports and is satisfactory considering the ultra-small dimension of the NPs.[57] However, BF-TEM size analysis is based on a limited number of NPs in dry conditions. Therefore, to test the aggregation state and the stability in aqueous environments and to account for a larger number of NPs, we performed SAXS measurements (Fig. 1d and S2a), which also provide valuable information on the hydration shell and the stabilizing agents. The size distribution by volume shows that the a-NPs have an average radius of 1.9 ± 0.7 nm, while the average radius of the t-NPs was determined to be about 1.3 ± 0.3 nm for the t-NPs (Fig. 1e and S2b, respectively). Most probably, the discrepancy between TEM and SAXS is due to the limits of TEM analysis, which does not allow for the detection of the hydration shell and the thin organic coating around the NPs. Nevertheless, SAXS analysis confirms that the NPs do not aggregate, even considering

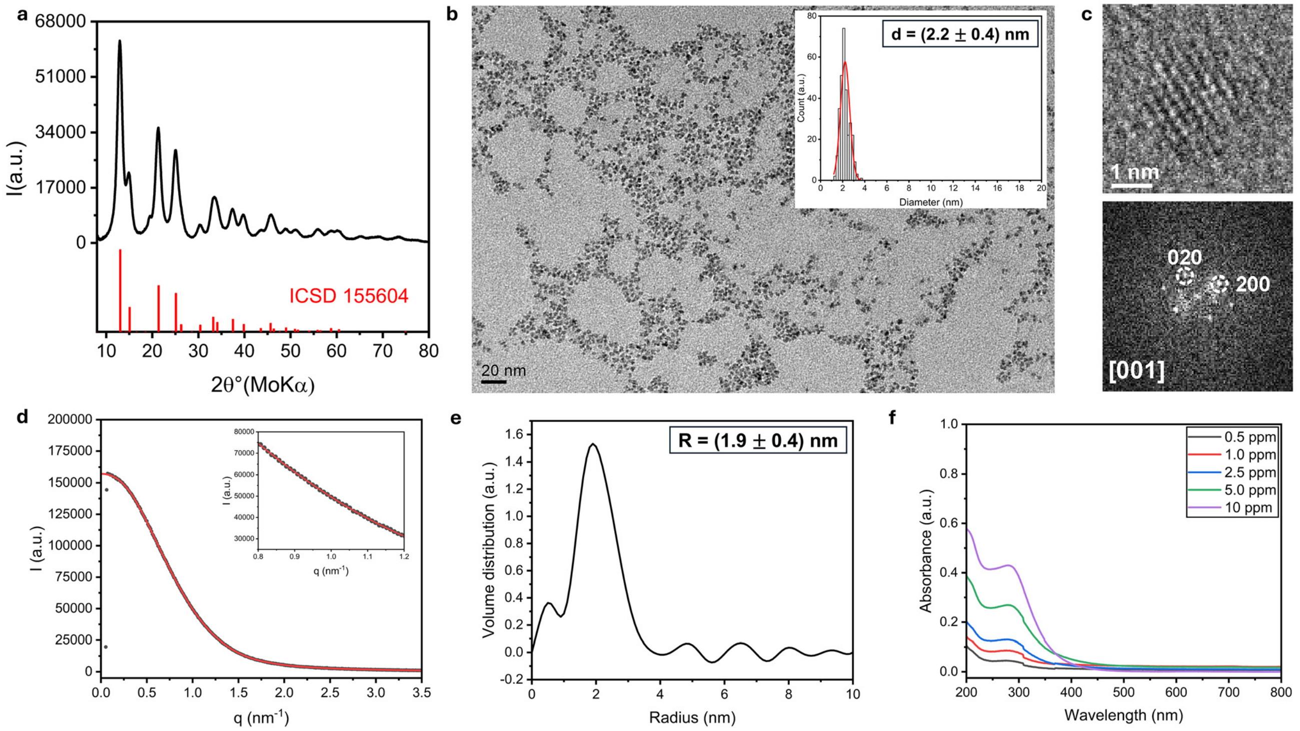

Fig. 1 (a) XRD pattern of CeO_2 NPs with the corresponding reference peaks. (b) BF-TEM image of a-NPs with the corresponding size distribution (inset). (c) HRTEM image and the corresponding FFT of an individual a-NP, indexed based on cubic CeO_2 (ICSD 155604). (d) Experimental curve (black dots) and fit (red line) of the SAXS data of a-NPs (inset: zoomed-in portion of the graph). (e) Size distribution by volume of a-NPs obtained from SAXS measurements. (f) UV-visible spectra of a-NPs at different concentrations.

a vast number of NPs. This result is highly relevant for the application of the NPs in different fields as the absence of aggregation guarantees that all the surface area is available for the catalytic activity. Additionally, SAXS measurements were repeated after 6 months from the preparation of the NPs and the same average radius was determined for both the a-NPs and t-NPs within the experimental uncertainty (Fig. S2c–f). This advanced characterization demonstrates that we have achieved significant stability of the NPs in an aqueous dispersion, an important factor for their effective use in long-term applications. Furthermore, the ultra-small size achieved with this scale-up protocol is pivotal because it leads to maximizing the surface-to-volume ratio, and, hence, to a marked increase in the number of available active sites on the surface.

To further study the surface structure of the NPs, HRTEM was employed since it provides information on the shape and the crystal structure at the nm scale. As can be observed in Fig. 1c and S1c, both a-NPs and t-NPs are isotropic (*i.e.*, they are not enclosed by extended facets). Strain analysis on XRD data confirms this observation. Crystal strain was estimated to be 0.78 ± 0.06% with a refined lattice parameter of 5.434 ± 0.004 Å. Lattice strain is generally correlated to the formation of defects which, in CeO_2 NPs, mainly correspond to the formation of oxygen vacancies.[58] In particular, strain is expected in ultra-small NPs due to the high concentration of Ce(III) on the surface; furthermore, the surface takes on a major role due to the increased surface-to-volume ratio.[59]

The presence of Ce(III) and Ce(IV) ions in CeO_2 NPs can be determined through UV-visible spectroscopy. The trivalent cation generally absorbs in the range of 230–270 nm, while the absorbance of Ce(IV) falls at higher wavelengths, 300–400 nm.[60,61] As shown in Fig. 1f and S3, the spectra of both the a-NPs and t-NPs have characteristic bands, indicating the simultaneous presence of both oxidation states in the NPs. Nevertheless, precise quantification is quite complex with this technique because the characteristic peaks are partially superimposed, and the simultaneous presence of both oxidation states could only be determined in solution.

The relative Ce(III)/Ce(IV) ratio was deeply investigated through environmental XPS in order to confirm the highly sub-stoichiometric character of the NPs and gather quantitative information. The XPS characterization was focused on Ce 3d peaks, which include both Ce(III)- and Ce(IV)-related signals. In particular, U-type peaks are related to $3d_{3/2}$, while V ones are related to $3d_{5/2}$. V_0, V′, U_0, and U′ (880.9, 885.2, 899.1, and 903.4 eV) represent Ce^{3+} species, while V, V″, V‴, U, U″, and U‴ (882.7, 888.5, 898.3, 901.3, 907.3, and 916.9 eV) are characteristic of Ce^{4+} species.[62,63] All analyzed samples present a mixed valence state while having a slightly higher percentage of Ce^{4+}. In the a-NPs, Ce^{3+} amounts to 46.3%, when the measurement is performed under an Ar atmosphere (Fig. 2a). Similar values were obtained for the t-NPs, where Ce(III) amounts to 41.9% (Fig. S4). These results agree with previous observations regarding crystal strain in ultra-small CeO_2 NPs.

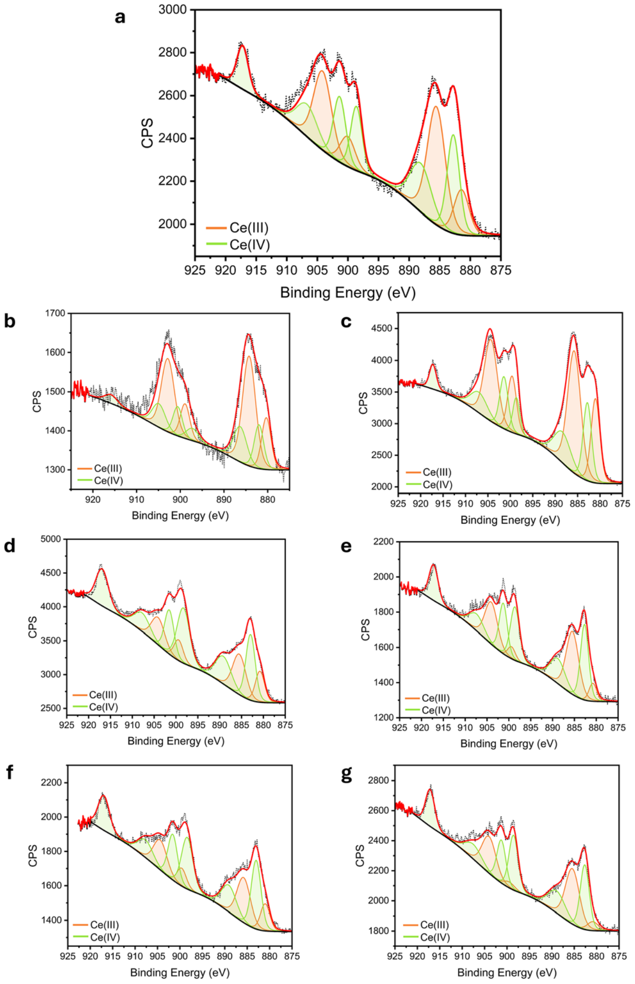

Fig. 2 Ce 3d region of a-NPs where Ce(ɪɪɪ) (orange) and Ce(ɪᴠ) (green) have been fitted. The measurements were performed for the NPs deposited and dried on a silicon wafer under the following conditions. (a) Under an Ar atmosphere. (b) Under an Ar atmosphere after 3 months of exposure to natural light. (c) Under an Ar atmosphere after heating the NPs to 300 °C on a button heater. (d) Under an O_2 atmosphere. (f) Under an Ar atmosphere after adding H_2O_2 (H_2O_2/NPs ratio: 1 : 2). (e) Ce 3d region of a-NPs acquired in aqueous solution with an *ad hoc* engineered cell system. (g) Ce 3d region of a-NPs acquired in solution with H_2O_2.

Considering that the a-NPs and t-NPs do not present significant differences in terms of physico-chemical properties and catalytic activity (as described in Fig. S5a and S5b), the following investigations will be focused on the a-NPs, due to the advantages related to the reduced toxicity of NH_4OH.

Redox cycling and related catalytic activity of CeO_2 NPs

In order to establish a clear structure–function relationship in the NPs, the physico-chemical characteristics need to be correlated to the redox cycling that can be established on the surface of the NPs. Indeed, the reversible conversion between Ce(ɪɪɪ) and Ce(ɪᴠ) is linked not only to crystal strain and the ultra-small size of the NPs, but also to the catalytic properties. For this reason, we deepened the characterization by investigating how the Ce(ɪɪɪ)/Ce(ɪᴠ) ratio changes when the nanocatalyst is subjected to different factors.

This study leverages on the unique features of environmental XPS, which provides information on the samples analyzed under conditions similar to the environmental ones. Indeed, the acquisition was not performed in a high vacuum. Instead, the measurements were performed at a pressure that was closer to the atmospheric one compared to standard instruments, allowing us to gain information on the sample in solution. In this work, the main parameters under investigation are light, high temperature (300 °C), an O_2 atmosphere (as opposed to the conventional Ar atmosphere), and H_2O_2. Light exposure leads to an increase in the percentage of Ce^{3+} to 64.9% (Fig. 2b), while a significant temperature increase induces an increase to 62.2% (Fig. 2c). Differently, the NPs that were studied under an O_2 atmosphere show an opposite trend. Under the O_2 atmosphere, the percentage of Ce^{3+} in the deposited NPs decreases to 32.2% (Fig. 2d) and the same effect can be observed when the measurement is performed in an ultrapure water solution (decrease to 38.9%, Fig. 2e). This shows the dependence of the Ce(ɪɪɪ)/Ce(ɪᴠ) ratio on the environmental conditions, which can be both reducing (*i.e.*, light and temperature increase) and oxidizing (*i.e.*, O_2 influence). Consequently, the starting Ce(ɪɪɪ)/Ce(ɪᴠ) ratio can be restored simply by interacting with commonly present environmental factors. This observation allows us to further comment on the regeneration potential of the nanocatalyst. Indeed, its performance in catalytic applications is strongly related to the stoichiometry of Ce atoms at the surface of the NPs.[64,65] The activity is influenced by the presence of Ce(ɪɪɪ) and the formation of surface defects in the form of oxygen vacancies.[66] Consequently, the regeneration potential of the nanocatalyst due to the opposite effects of different environmental factors opens the way to long-term efficiency of its protective action.

In the specific case of the oxygen-related activity of the NPs, the catalytic activity resembles an enzyme-like behavior with CeO_2 NPs presenting both peroxidase- and oxidase-like activities. In the first case, the NPs can decompose H_2O_2 to finally produce water, while in the second case, the NPs interact with O_2 to generate either H_2O_2 or H_2O. Considering this activity and how it could be exploited to exert a protective action in the coating, we investigated how the interaction with both species can influence the Ce(ɪɪɪ)/Ce(ɪᴠ) ratio. As discussed, an O_2 atmosphere and an ultrapure water solution can have an oxidizing effect on the NPs, decreasing the amount of Ce(ɪɪɪ). Additionally, we used environmental XPS to study how the Ce(ɪɪɪ)/Ce(ɪᴠ) ratio changes when the NPs interact with H_2O_2. First, the measurements were performed after adding H_2O_2 to the NPs that were previously deposited and dried on a silicon wafer. Then, tests were repeated in an aqueous solution containing H_2O_2. In both cases, the Ce^{3+} percentage decreases to 34.3% for the deposited NPs (Fig. 2f) and to 37.5% in solution (Fig. 2g). We then expanded on these results by assessing the peroxidase- and oxidase-like activities of the NPs. This investigation allows to determine the effect of the NPs on oxygen-based species and provides information on the concentration

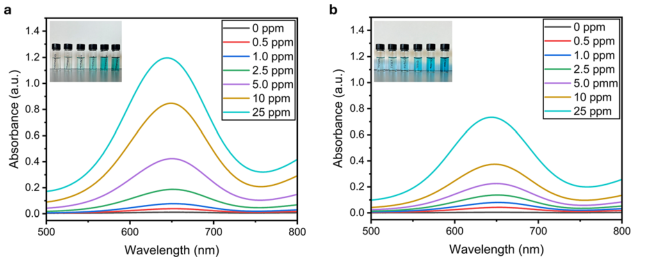

Fig. 3 (a) Peroxidase-like activity of a-NPs determined in an ultrapure water solution by studying their interaction with H_2O_2 in the presence of TMB. (b) Oxidase-like activity of a-NPs determined in an ultrapure water solution by studying their interaction with O_2 in the presence of TMB.

at which the NPs are active, and the time needed to observe an effect.

The tetramethylbenzidine (TMB) assay was employed to test the performance of different concentrations of the NPs, and the results are presented in Fig. 3a and b. The optimal reaction time was chosen by evaluating the onset of the plateau region at which the maximum concentration of the oxidized form of TMB is reached. Measurements were performed at different NPs' concentrations, ranging from 0.5 to 25 ppm, proving that the minimum concentration at which a signal can be detected is 1 ppm. The result is in agreement with the ultra-small size of the NPs, which endows them with a larger surface area for the catalytic activity.

Biocompatibility assessment

The formulation of a coating based on CeO_2 NPs needs to take into account any health and safety concerns that the components of the coating might pose. In the case of the formulation proposed in this work, chitosan was selected as a sustainable and biocompatible matrix. Its biodegradability and recognized safety make it an optimal alternative to formulate biocompatible coatings.[67–70] Instead, the potential toxicity of CeO_2 NPs should be explored. Indeed, considering the ultra-small dimension and the enzyme-like activity of the NPs, it is fundamental to investigate how these properties can impact the interaction with cells, since a decrease in NPs size and a strong reactivity can alter their biocompatibility profile by impairing cellular metabolism. Taking into account these facts, we performed cell viability assays on the a-NPs and t-NPs to confirm that they can be used without health concerns, in alignment with the "Safe-by-Design" approach. Given the critical role of the NPs' biological identity,[71] we first focused on the influence of the protein–NPs interaction on the physicochemical properties and stability of the NPs, which substantially affect their biological identity within cellular systems. We incubated the NPs in an FBS-rich aqueous solution to form a protein coating around them and measured the hydrodynamic diameter. The interaction with proteins leads to a 10-fold increase in the size of the NP–protein conjugates, as depicted in Fig. S6a and S6b. Furthermore, we assessed the changes in the average hydrodynamic diameter of the NPs after incubation in the cell culture medium, in which high ionic strength and high protein concentration are simultaneously present; the diameter was measured at different time points from a few minutes to 72 hours. These results demonstrate that, after a slight decrease in the first 24 hours, the hydrodynamic diameter of the a-NPs remains constant for up to 72 hours (Fig. 4a and b). These data demonstrate that the a-NPs have good stability in the cell culture medium and that there are no signs of aggregation phenomena. To establish a comparison with previous stability assessments present in the literature, we measured the changes in the hydrodynamic diameters of two commercial CeO_2 NPs that remain unchanged or slightly increase in the 72 hours (Fig. 4a and b).

After this evaluation, the *in vitro* cytotoxicity of CeO_2 NPs was investigated with two different methods: the PicoGreen assay and the LIVE/DEAD assay. The PicoGreen assay was performed at 24 and 72 hours of NPs incubation. As shown in Fig. 4c and S7, the fluorescence signal does not change significantly at either exposure times, indicating that the NPs do not exert significant cytotoxic activity even at concentrations of

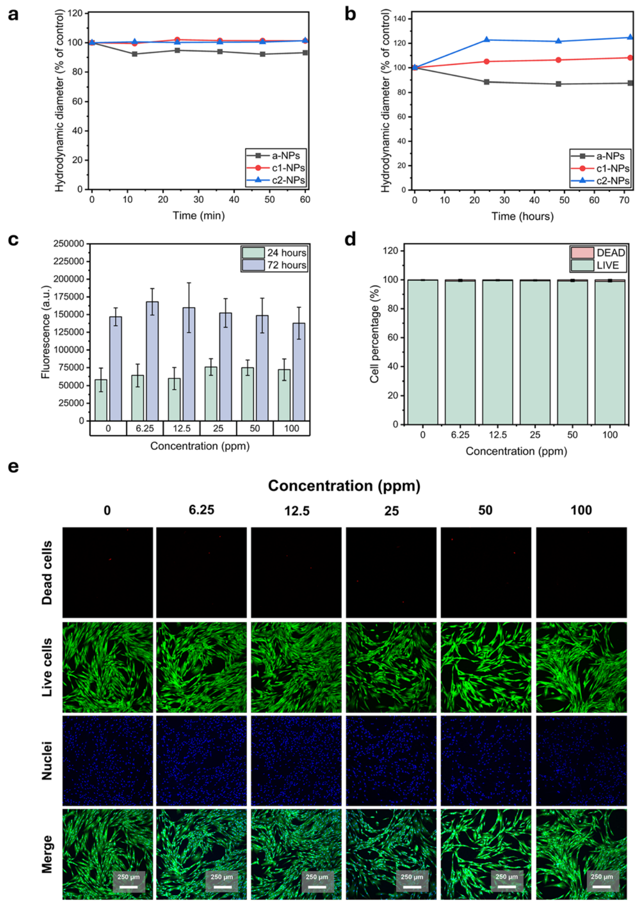

Fig. 4 (a and b) Short- and long-term stability assays of a-NPs and two types of commercial CeO_2 NPs. (c) PicoGreen assay of a-NPs at two different exposure times, 24 and 72 hours. (d) Quantitative analysis of the data obtained through the LIVE/DEAD cell viability assay. (e) Representative confocal images of primary normal human dermal fibroblast cells acquired during the LIVE/DEAD cell viability assay.

100 ppm. We confirmed these results with a LIVE/DEAD assay, which further demonstrates a cell viability of almost 100% after 72 hours of treatment for all the tested NPs' concentrations (Fig. 4d and e). These results are in line with previous assessments on the biocompatibility of CeO_2 NPs.[72,73]

To further establish the influence of the NPs' size on the interaction with cell membranes and internalization pathways, we performed internalization tests by means of ICP-MS. The treated cells have a concentration of about 1.03×10^{-8} ng, indicating a very modest internalization compared to what was observed in the literature for larger CeO_2 NPs (commercial, >25 nm, and synthesized, 8 nm).[72,73] This result represents an important observation and requires further in-depth investigation. Indeed, the exceptional stability of the NPs could possibly reduce their tendency to accumulate within cellular systems, thereby allowing continuous transfer in and out of the cells and avoiding the blockage of intracellular pathways. Moreover, a different factor affecting the uptake is possibly the protein adsorption on the surface of the NPs, which might be disfavored due to their small size.[74] Indeed, the formation of a stable protein-NPs system is generally hindered in ultra-small NPs due to their dimensions and this issue can affect the interaction with cells since the citrate coating could remain as the sole surface functionalization of the NPs. It has been demonstrated by Epple *et al.* that the presence of carboxylic groups as end groups on the surface can strongly limit the uptake in cells.[74] Therefore, considering these observations regarding the role of the NPs' surface properties, the carboxyl groups of citrate stabilizing the a-NPs could play a major role in limiting the internalization within cells.

Design and performance evaluation of the composite coating

Thanks to their high catalytic activity and potential for long-term protection, the NPs show promising features for application in multifunctional protective coatings in which they can provide both antioxidant and UV-shielding actions. Furthermore, we confirmed their biocompatibility, which makes them safe both for human health and for the environment. Nevertheless, NPs alone cannot be used as coatings because large quantities would be needed to completely cover the surface and the nanometric size would cause penetration in the highly porous substrates. In order to provide surface protection, the NPs need to remain catalytically active at the surface to shield the substrate from different environmental agents and counteract potentially damaging mechanisms. This poses a particular challenge in the case of porous substrates where it is inevitable for ultra-small NPs in aqueous dispersions to penetrate deep within the structure. For these reasons, the NPs should ideally be included in a filming matrix, such as a polymeric formulation. However, it is fundamental for the composite system not to hinder the catalytic activity of the NPs that act as the functional part of the protective formulation. In this work, we decided to introduce CeO_2 NPs in a chitosan formulation to form a composite material. We selected chitosan as it provides a barrier effect and filming properties, whilst being overall more sustainable than conventionally used synthetic polymers. Recently, CeO_2 NPs and chitosan have been explored to produce composite films for food packaging and wound dressing applications. The publications on the topic impact different fields and show that the synergy between the NPs and the polymeric matrix can lead to multifunctional composites.[75–77] These early works focus on the thermal and mechanical properties of the films, while only marginally exploring antioxidant and antimicrobial properties. Considering the aim of our work, we plan to move the focus on the surface characterization and protective capability of the polymer nanocomposite, exploring a novel application for this composite. The concentration of the polymer in this formulation is crucial as it imparts specific rheological characteristics, which can in turn affect the filming properties of the substrate and the ease of application.

Leveraging on previous results,[56] we tested chitosan formulations with chitosan concentrations of 0.2% w/v (cs02), 0.4% w/v (cs04), 1.0% w/v (cs1) and 2.0% w/v (cs2). As depicted in the SEM images presented in Fig. S8a–d, the increase in chitosan concentration does not significantly change the morphology of the coating; however, cs2 shows some fibrous portions which were not visible in the other samples. In terms of rheological properties, the viscosity of all formulations increases compared to cs02 (Table S1). These considerations are important to determine the most suitable application method to apply the coating on the substrate. Given the high viscosity of formulations cs04, cs1, and cs2, we decided to use brush application rather than spray coating. Indeed, high viscosity of the coating would lead to longer application times in the case of spray coating and a viscous formulation could even clog the millimetric nozzle of the airbrush.

All the coatings were applied to fresco mock-ups, which require tailored strategies due to their complexity and to the intricate degradation processes they are subjected to. Indeed, these substrates are highly porous and multilayered, and they comprise both a mortar portion, mostly constituted of $CaCO_3$, and a painted plaster layer. The coating aims at protecting the outer layer, which consists of an inorganic pigment bonded to the surface through carbonation of the plaster beneath. While protection is the main goal of this coating, it is also important to avoid any modification of the aesthetic features of the mock-ups and to preserve water vapor permeability as much as possible.[78,79]

Considering this important point, the aesthetic features of the mock-ups were first monitored after the application of the coating. Table S2 shows the morphology and the color variation (*i.e.*, ΔE value) of the samples before and after the application of the coating. We did not measure significant color change even at high concentrations of chitosan, as the index always remained lower than 3 (the value below which the chromatic variation cannot be perceived by the naked eye).[80] By achieving significantly low ΔE values, we can confirm the transparency of our coating. Additionally, we studied the morphology of the surface through stereomicroscopy (Table S2). The microscopic images of the coated mock-ups confirmed that the morphology of the surface remains unaffected after the application of the coating.

In terms of hydrophobicity, the contact angle was evaluated, and the results are presented in Table S3. The uncoated sample is highly porous and immediately absorbs the water drop. Contrarily, the contact angle falls in the range of 40°–55° for all coated samples and a slight increase can be observed with higher concentrations of chitosan in the formulation. The higher value of contact angle compared to the uncoated sample indicates a more pronounced hydrophobicity of the coating, but the result could also be correlated to changes in the porosity of the surface layers. Indeed, when applying the coating, the pores closer to the surface might be partially clogged by the polymer, forming a film over the substrate. In order to quantitatively evaluate this effect, the protection factor and the water vapor permeability were also determined. On the one hand, the protection factor defines the capability of the substrate of absorbing water up to the maximum capacity and is generally used to express the protective performances of the coating. In our specific case, this parameter increases from the uncoated mock-up to the coated ones and provides the best results for cs2 (Fig. 5a). On the other hand, water vapor permeability is generally assessed by determining the water vapor resistance coefficient. This parameter should ideally be as close as possible to the one determined for the uncoated sample. High permeability of the coating is needed to avoid trapping stagnant water inside the treated substrate as it might lead to structural integrity issues in the long run. As shown in Fig. 5b, all the coatings we produced have a slightly lower permeation compared to the uncoated sample and the coefficient gradually decreases at higher polymer concentrations. Considering that water vapor permeability should be preserved, but at the same time the coating should provide a satisfactory barrier effect, a compromise needs to be found between these two factors. Taking into account this need, cs04 and cs1 were considered to be the best formulations since they represent a good balance of the two features. In contrast, cs02 and cs2 were excluded since they do not meet the requirements; cs02 does not provide a satisfactory barrier effect, while cs2 presents the lowest water vapor permeability of the tested formulations.

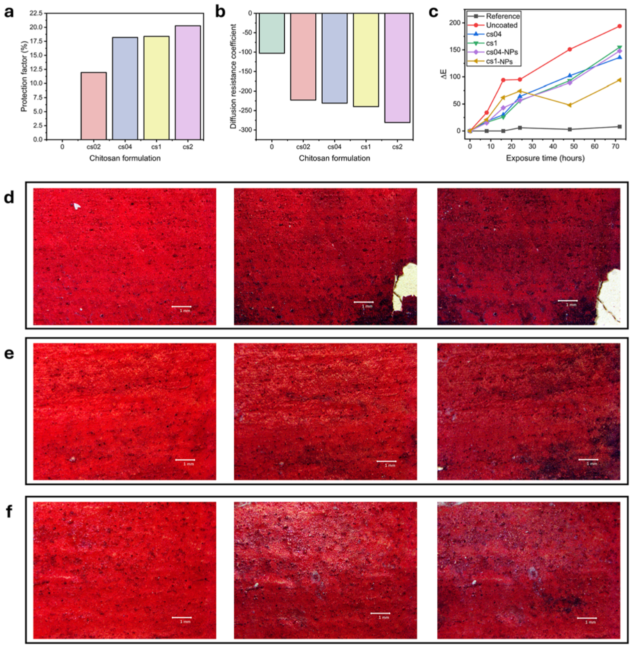

Fig. 5 (a) Protection factor of the four tested chitosan formulations after application on fresco mock-ups. (b) Water vapor permeability of the four tested chitosan formulations after application on fresco mock-ups, reported as a measure of the water vapor resistance coefficient. (c) Color variation of cinnabar fresco mock-ups coated with the cs04 and cs1 formulations with and without NPs, after different ageing times. (d–f) Microscopy images of the cinnabar fresco mock-ups before ageing (left), after 24 hours of ageing (center), and after 72 hours of ageing (right); uncoated mock-up (d), mock-up coated with cs04-NPs (e), and mock-up coated with cs1-NPs (f).

Taking into account these results, CeO_2 NPs were included in the cs04 and cs1 formulations, which can offer a barrier effect while guaranteeing surface permeability. To maximize the performances of the composite, we determined 25 ppm of NPs to be the ideal compromise to achieve optimal protective action while minimizing the amount of the nanomaterial used. In terms of protective action, the final concentration of 25 ppm was selected following the catalytic activity assessment. Indeed, the results from the investigation on the NPs' activity in solution showed that concentrations of tens of ppm of the nanocatalyst are sufficient to provide high activity. The so-prepared coating formulations (cs04-NPs and cs1-NPs) were then tested to evaluate their protective efficiency.

Fresco mock-up ageing and coating performance assessment

The CeO_2 NPs–chitosan coatings were applied to fresco mock-ups previously painted with cinnabar, a red HgS pigment. Alongside natural red earths, cinnabar was among the most prized pigments used by Greek and Roman artists, valued for its vivid and striking red hue. However, unlike natural earths, cinnabar was typically reserved for the most prominent spaces within elite residences, underscoring its high prestige and symbolic significance.[29,33,34] After archaeological excavation, gradual darkening of frescoes painted with cinnabar was evidenced as a consequence of exposure to light, high relative humidity and chlorine ions accumulated over time (Fig. S9a and S9b).[81,82] Unfortunately, until now, no coating strategy has been designed to prevent this color variation and, therefore, urgent action is needed to effectively tackle this problem. Taking into account the complexity of the system and the need for innovative approaches, we tested the ability of our protective coating to respond to the challenges posed by this system. To simulate the environment in which cinnabar degrades, the mock-ups coated with the protective nanocomposite formulation were exposed to a multifactorial deterioration pathway, as described by Neiman *et al.*[83] The complex degradation protocol mimics the typical deteriorating environment surrounding cinnabar-painted frescoes and involves the simultaneous exposure to UV radiation, high relative humidity and chlorine-based salts.

The degradation mechanisms leading to the color change remain debated (Fig. S10), but three main hypotheses have been suggested: (1) the formation of photosensitive chlorine-based species, (2) the establishment of photoinduced redox processes, and (3) the phase transition between cinnabar (a-HgS) and metacinnabar (b-HgS).[31,84–87] In the last decade, the simultaneous occurrence of these processes has also been proposed. Radepont *et al.* suggested that both metallic mercury and chlorine-based species such as cordierite (a-$Hg_3S_2Cl_2$) and calomel (Hg_2Cl_2) can be formed as a consequence of the reaction between a-HgS and gaseous ClO.[88] The formation of Hg(0) is a consequence of the mentioned redox process through which the sulphide ion can be converted into S(0) or even sulphate, at the same time as the mercury is reduced. The process is still chlorine-dependent since this species acts as a catalyst in the redox mechanism. As determined in two works that tackled this issue in the last 5 years,[89,90] the experimental proof of this mechanism is extremely challenging due to instrumental limitations. Indeed, the high vacuum required during XPS characterization can potentially cause the evaporation of Hg(0), making the presence of sulphate the only indication of a redox reaction happening.[89] At the same time, the distinction between cinnabar and metacinnabar is challenging as they share the same elemental composition, making them undistinguishable in elemental characterization. Moreover, they have similar peaks in Raman spectra and the distinction generally requires techniques with high spatial resolution.[90] The current instrumental limitations are probably at the root of the debate, since clear identification of different species is fundamental to distinguish between several degradation pathways. In order to ascertain the mechanism involved in the present case study, we degraded an uncoated cinnabar-painted mock-up, and we performed both micro-Raman and XPS analyses. The results confirmed the experimental limitations previously reported in the literature (Fig. S11a, S11b and S12a–d).

Considering the different mechanisms that have been proposed for the blackening of cinnabar, the protective strategy should provide a UV-shielding action, while at the same time blocking the redox mechanisms that can be catalyzed by the presence of chlorine-based species. CeO_2 NPs can act on both fronts thanks to their antioxidant activity and UV-shielding characteristics, which are also enhanced by the presence of a chitosan matrix. After the application of the two formulations to mock-ups and their simultaneous exposure to UV radiation and NaCl solution, we could confirm that the coating is able to inhibit the degradation of cinnabar and its consequent blackening. By monitoring the chromatic variation of the samples, it is clear that the color variation of the coated mock-ups is inferior compared to the uncoated sample (Fig. 5c and Table S4). cs1-NPs achieve higher performances, as the only significant color variation happens within the first 8 hours of exposure. Differently, the uncoated sample shows great color variation at all steps of the degradation process and, after 72 hours, it presents the highest value of ΔE. These observations confirm the positive effect of the NPs against the degradation caused by these environmental conditions. The microscopy images confirm these results, determining that the blackening of the coated samples is slowed down or even completely prevented thanks to the presence of the coating (Fig. 5d–f). Pictures of the complete mock-ups (Table S5) further demonstrate the protection achieved thanks to the coating. Indeed, as clearly visible, black spots are already present on the uncoated sample after 8 hours of ageing. Contrarily, black spots are formed in a small amount for the mock-up coated with cs04-NPs after 16 hours of ageing, whilst in the sample coated with cs1-NPs they cannot be observed at all even up to 48 hours of ageing. The improved performance of cs1-NPs compared to cs04-NPs could be related to the different penetration of the coating in the porous substrate and, hence, to the different amount of the NPs present at the surface. Indeed, since cs04-NPs is less viscous, it is likely to partially enter the porous structure of fresco mock-ups, reducing the amount of functional nanomaterials present at the surface and protecting the pigment. These considerations show that the rheological and filming properties of the cs04 formulation are not suitable for application on highly porous materials. The same conclusions can be drawn from the comparison between the protective ability of CeO_2 NP-based coatings and that of cs04 and cs1, without the addition of the NPs. While the addition of NPs to cs1 leads to clear improvements in its protective ability, the role of the NPs in cs04 appears to be marginal (Table S5). Both cs04 and cs04-NPs start to fail after about 16 hours of ageing, suggesting that the NPs are not exerting any protective action. The effect can be attributed to the unsuitability of the cs04 polymeric matrix in confining the NPs at the surface.

Considering the successful results achieved with the cs1-NPs formulation, we extended the investigation to a real case study by testing the effectiveness of the coating on precious fresco fragments from the archaeological site of Aquileia (Italy). Cinnabar was identified in both the tested fragments, as confirmed from the Raman spectrum presented in Fig. S13. In Fig. 6, the comparison between the coated and the uncoated samples exposed to the same ageing protocol confirms the protective action of the coating. While a distinct darkening can be observed on the uncoated surface, no changes were detected on the coated fragment. This opens the application of the coating to the crucial task of frescoes' protection in important archaeological sites, where outdoor conditions constantly threaten their conservation.

The effectiveness of the cs1-NPs coating in protecting the substrate from darkening determines that the synergy between the NPs and the biopolymeric matrix has been successfully achieved. Furthermore, the effective protection achieved by using only 25 ppm of the nanocatalyst shows that we have overcome important hindering effects of the catalytic sites that the organic biopolymeric matrix might have provoked. With this result, we show that we have effectively overcome the limitations related to the introduction of CeO_2 NPs in organic formulations that were reported in previous works.

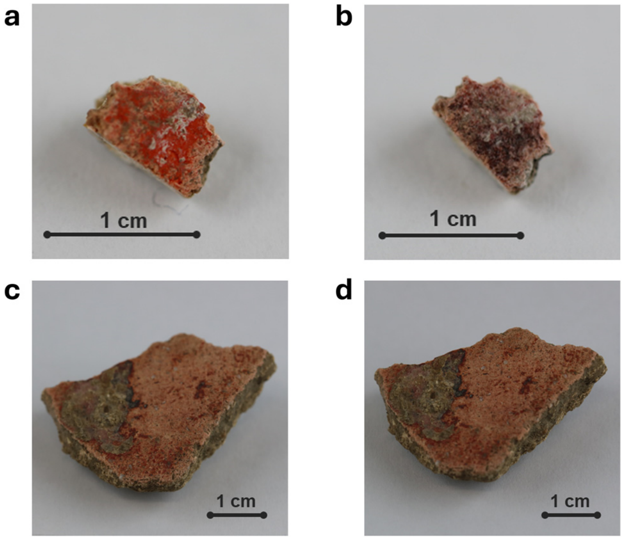

Fig. 6 (a) Uncoated fresco fragment before the degradation protocol. (b) Uncoated fresco fragment after simultaneous exposure to UV light, chlorine-based salts, and high relative humidity. (c) Fresco fragment coated with cs1-NPs before the degradation protocol. (d) Fresco fragment coated with cs1-NPs after simultaneous exposure to UV light, chlorine-based salts, and high relative humidity.

Conclusions

In this work, we successfully developed a functional coating able to protect complex substrates from deterioration pathways induced by exposure to a multifaceted environment. In particular, we designed a microwave-assisted synthesis method to produce ultra-small CeO_2 NPs with an enhanced surface-to-volume ratio and high colloidal stability. Our protocol yields citrate-coated, non-stoichiometric NPs, with a remarkable content of Ce(III), endowing the nanocatalysts with exceptional antioxidant properties and versatility. We have established a well-defined structure–function relationship by demonstrating the Ce(III)/Ce(IV) redox cycling of the NPs using *in situ* environmental XPS and linking the results to the catalytic performances. This approach represents a significant advancement, as we have achieved precise and reproducible control over the surface chemistry and redox properties.

Furthermore, we leveraged the synergistic interaction between the NPs and chitosan to develop a protective composite coating that offers superior barrier properties alongside prolonged antioxidant activity. We demonstrated that the NPs-based catalytic shield successfully prevents the complex degradation processes of cinnabar induced by the combined exposure to UV light, chlorine-based salts, and high relative humidity.

In summary, this strategy delivers efficient and multifactorial protection, highlighting the potential of ultra-small CeO_2 NPs-based composites as high-performance coatings for a wide range of technological applications.

Experimental

Synthesis of CeO_2 NPs

Cerium(III) nitrate hexahydrate [$Ce(NO_3)_3·6H_2O$], sodium citrate tribasic dihydrate, ammonium hydroxide solution (NH_4OH, 28.0–30.0%), and tetramethylammonium hydroxide solution (TMAOH, 10%) were purchased from Sigma-Aldrich (Merck). All chemicals were used as received without further purification and ultrapure water (Millipore system) was used for all syntheses. The microwave-assisted synthesis was designed starting from a previously published protocol.[57] Briefly, $Ce(NO_3)_3·6H_2O$ (0.1 mmol) and sodium citrate (0.2 mmol) were mixed with 5 mL of ultrapure water and stirred until complete solubilization. NH_4OH (or TMAOH) was added to reach a pH of 10. The solution was then stirred overnight at room temperature. The hydrothermal protocol was implemented in a Milestone Ethos UP microwave system (Milestone srl, Bergamo, Italy), utilizing a multi-vessel system in which the temperature was increased to 100 °C over 15 minutes and maintained for 30 minutes. Subsequently, the vessels were allowed to cool down to 50 °C over 20 minutes before being removed. Following 2 hours of cooling to room temperature, the final products were purified using Amicon® Ultra membrane filters (3 K).

Chitosan formulation optimization

Chitosan (cs, medium molecular weight), lactic acid (≥85%), azelaic acid (98%), sodium hydroxide (NaOH, ≥98%), and glycerol ($HOCH_2CH(OH)CH_2OH$, 99.0–101.0%) were purchased from Sigma-Aldrich (Merck). All chemicals were used as received without further purification and ultrapure water (Millipore system) was used for all preparations. Starting from a published work,[56] a chitosan formulation was optimized by increasing the concentration of the biopolymer to achieve better filming properties and barrier effect. To summarize, azelaic acid (28 wt% on a chitosan basis) was added to 50 mL of ultrapure water and the mixture was stirred until complete dissolution. Chitosan was added in different amounts to reach a concentration of 0.2% (w/v), 0.4% (w/v), 1.0% (w/v), and 2.0% (w/v), respectively, for each formulation. The mixture was then heated to 95 °C while stirring at 600 rpm and lactic acid (60 wt% on a chitosan basis) was added once the temperature was reached. The mixture was allowed to cool down and then glycerol was added. In order to neutralize the formulation, a 0.3 M solution of NaOH was added until the pH reached 8.

Fresco mock-up preparation and coating

In order to test our coatings on samples replicating as much as possible the complexity of frescoes, we produced fresco mock-ups starting from historical Vitruvius recipes, while also simplifying the preparation process to facilitate high-throughput screening of the coatings. Natural cinnabar (#10620) and marble dust (powder, <200 μm) were purchased from Kremer Pigmente, while lime putty and coarse quartzite (0.1–0.3 mm) were acquired from CTS Conservation. Coarse-grained river sand (0–1 mm) from AXTON was purchased from Leroy Merlin.

The simplified samples were obtained by solely reproducing the outer layers of frescoes, *i.e.*, the *intonachino* covered by the pigment layer. In particular, we employed laboratory glass slides as a support for the mortar layer, and we wrapped a gauze strip (10 cm × 5 cm) around it to guarantee good gripping. We prepared *intonachino* by mixing marble dust and lime putty in a 1 : 1 ratio and by adding water when necessary. We applied the *intonachino* on the support and we painted it with cinnabar dispersed in ultrapure water before it dried, following the traditional fresco technique. The mock-ups were allowed to carbonate for 3 months.

Complete fresco mock-ups were also prepared to test the protection factor and the water vapor permeability of the coatings. The procedure for the outer layers remains the same as the one described for the simplified mock-ups. However, beneath the *intonachino* layer, the *arriccio* layer was first prepared. *Arriccio* was obtained by mixing lime putty, coarse quartzite and coarse-grained river sand in a 1 : 1 : 1 ratio and adding enough water (q.s.) to achieve adequate workability of the mortar. The mock-ups were allowed to carbonate for 6 months.

The two types of mock-ups are schematically represented in Fig. S14. After carbonation, they were coated with the chitosan formulations or with the composite CeO_2 NPs-based chitosan formulations by brush painting (0.125 mL cm^{-2}).

Characterization of CeO_2 NPs

X-ray diffraction (XRD) patterns were acquired with a Malvern PANalytical third-generation Empyrean X-ray diffractometer, operating at 60 kV and 40 mA and equipped with a 2.5 kW Mo Kα X-ray tube and a GaliPIX3D solid-state pixel detector. The diffraction pattern was obtained in transmission geometry from 8° to 80° with a step size of 0.043° and a scan speed of 1.2° min^{-1} using a Mo focusing mirror, a reflection–transmission spinner sample stage (rotation speed = 1 rps) and 5 μm Mylar foil as the sample substrate. Size and strain analysis was performed using HighScore Plus 5.3 software and the whole-powder-pattern decomposition (WPPD) technique based on the Pawley algorithm. The instrumental broadening was removed using a diffraction pattern obtained from the NIST LaB_6 (SRM 660) standard. The characterization was performed in powder form: 1 mL of CeO_2 NPs dispersion was freeze-dried overnight to remove the solvent.

Bright-field transmission electron microscopy (BF-TEM) analyses were performed using a JEOL JEM-1011 microscope with a thermionic source (W filament), operating at 100 kV. TEM images were analyzed using the software ImageJ to determine the average diameter of the NPs; in each image, the diameter of 100 NPs was measured to obtain an average value. A small volume of each sample diluted 1 : 1 with methanol was drop-cast onto carbon/Cu grids (300 mesh). To investigate the crystallinity at the nanoscale, high-resolution TEM (HR-TEM) was performed using an image Cs-corrected JEOL JEM-2200FS TEM, equipped with an in-column image filter (Ω-type), operating at 200 kV. The HR-TEM images presented here were acquired using a direct electron detection camera (K2 Summit, Gatan), so as to reduce beam damage (*e.g.*, carbon contamination build-up). A small volume of each sample was drop-cast onto ultrathin carbon/holey carbon/Cu grids. Then, small-angle X-ray scattering (SAXS) analysis was performed using a Malvern PANalytical third generation Empyrean multipurpose platform in transmission geometry with Cu Kα radiation (λ = 1.54 Å; 40 kV, 45 mA). 1D-SAXS measurements were carried out in a vacuum path chamber (Scatter X78) using a beam with line collimation and a GaliPIX3D detector. Quartz capillaries (Hilgenberg, DE) with 1 mm diameter (100 μL volume) were used. Background measurement of ultrapure pure water was performed in the same capillary used for the NPs dispersions. Scans were performed in the q region of 0.1–3.5 nm^{-1} with a step size 0.014°, with an exposure time of 30 min. Data analysis was performed using EasySAXS software (Malvern PANalytical). The software performs primary data handling steps, including absorption correction, background subtraction, and conversion of the scattering angle 2θ to the scattering vector q. Determination of NPs distribution was performed using an indirect integral transform technique that relates experimental SAXS data to the volume distribution function $D_v(R)$ using a regularization procedure.

Redox cycling of CeO_2 NPs

Environmental X-ray photoelectron spectroscopy (XPS) was used to determine the relative Ce(III)/Ce(IV) ratio on the surface of the NPs and to study how this ratio evolves when the NPs are subjected to different oxidizing and reducing agents (*i.e.*, O_2, H_2O_2, UV radiation, and high temperature). For this analysis, we used an EnviroESCA system (SPECS Electron Spectroscopy for Chemical Analysis Under Environmental Conditions, GmbH, Germany) with a monochromatic Al Kα X-ray source (1486.71 eV), present at Charles University, Prague. The analyzer (SPECS PHOIBOS 150) operates under ultra-high vacuum conditions (10^{-9} mbar), and signal detection was conducted in FAT (fixed analyzer transmission) mode.

During the XPS measurements, the core-level spectra of Ce 3d, Na 1s, C 1s, and O 1s, and the valence band were recorded with a pass energy of 20 eV, a step size of 0.1 eV, and a dwell time of 0.3 seconds. Both the fresh NPs and the ones exposed to natural light for 3 months under conventional laboratory conditions were drop-cast on silicon wafer substrates and analyzed under a 1 mbar Ar atmosphere with a flow of 25 mL min^{-1} during the measurement. The same measurement was repeated for the fresh NPs under an O_2 atmosphere and then the NPs were treated with a 1 M solution of H_2O_2 (10 : 1 ratio) and analyzed under an Ar atmosphere. Lastly, the NPs were drop-cast onto CHU01 (cooling heating unit), which was connected through the EnviroESCA interface. The temperature was monitored using a thermocouple on the heating unit, which was heated up to 300 °C. The spot size was 200 μm.

Through an *ad hoc* engineered cell system,[91] the Ce(III)/Ce(IV) ratio of the NPs was investigated in an ultrapure water solution, in the presence or absence of H_2O_2. The binding energy scale was referenced to the Ce^{4+} $3d_{3/2}$ U^{III} peak at 916.7 eV and spectra elaboration was then carried out using CasaXPS software (2.3.25 version). An U2 Tougaard background was applied across the binding energy range of the peaks of interest.

Oxygen-related catalytic activity of CeO_2 NPs

Hydrogen peroxide (H_2O_2, 30%) was purchased from Sigma-Aldrich (Merck). 3,3′,5,5′-Tetramethylbenzidine (TMB) was obtained from Kementec, Denmark. All chemicals were used as received without further purification and ultrapure water (Millipore system) was used for all solution preparations. TMB was employed as a chromogenic substrate to investigate the peroxidase- and oxidase-like activities of CeO_2 NPs. The peroxidase-like activity was determined by using H_2O_2 as a substrate in a system containing a mixture of TMB and H_2O_2 (1 M) at a 1 : 1.6 ratio. The oxidase-like activity was tested by using molecular oxygen dissolved in water from the atmosphere as a substrate.

In both cases, the characteristic peak of the oxidized form of TMB at 652 nm was monitored by obtaining the UV-visible spectra using a double beam Agilent Cary 100 Series UV-Vis spectrophotometer (Agilent Technologies, Santa Clara, CA, USA) at room temperature. The spectra were obtained in the 800–200 nm range using CaryWinUV Scan software (4.20 version). They were then elaborated using OriginPro 2022 software (OriginLab Corporation, Northampton, MA, USA). UV-visible spectra are presented in the range of 500–800 nm, which is the region where the mono-oxidized form of TMB absorbs. This region is otherwise free of signals, as can be observed from the UV-visible spectra of the NPs presented in Fig. S4a and S4b.

The effect of CeO_2 NPs concentration and the kinetic trend of this interaction were studied; the activity was tested in the concentration range of 0.1–25 ppm, including the control test of the chromogenic substrate in the absence of the nanocatalyst (0 ppm). The spectra were obtained 5, 10 and 15 min after the addition of TMB.

Biocompatibility assays of CeO_2 NPs

The stability of the NPs was compared with two commercial ones (cerium(IV) oxide 20% in H_2O, <5.0 nm, Alfa Aesar; cerium(IV) oxide nanopowder, <25 nm, Sigma-Aldrich). In order to study the interaction between proteins and CeO_2 NPs, they were incubated for 2 h at room temperature and under mild agitation in an aqueous solution containing 50% heat-inactivated fetal bovine serum (FBS, Gibco). Subsequently the NPs were rinsed to remove any unbound serum proteins.

A stability assay in cell culture medium was performed on 100 ppm dispersions of the NPs. We used Dulbecco's modified Eagle's medium (DMEM, Gibco) supplemented with 20% of heat-inactivated fetal bovine serum (FBS, Gibco), 1% L-glutamine (stock 200 mM, Gibco), and 1% penicillin–streptomycin (100 IU mL^{-1} of penicillin and 100 μg mL^{-1} of streptomycin, Gibco). In these analyses, the hydrodynamic diameters (d_h) were analyzed over 1 h with single acquisition every 12 min and over 72 h with acquisitions every 24 h. For the determination of the average d_h, dynamic light scattering measurements were performed using a Malvern Zetasizer Nano ZS90 instrument. The values were assessed using a 100 ppm dispersion in polystyrene cuvettes.

The cytotoxicity effect of the CeO_2 NPs we synthesized was assessed *in vitro* using the PicoGreen assay (Quant-iT PicoGreen dsDNA Assay Kit, Invitrogen) that allows an indirect evaluation of cell proliferation through dsDNA concentration assessment. The cells were seeded in 96-well plates (Corning) at 10 000 cells per cm^2 and incubated overnight; thereafter, the cells were treated for 24 and 72 h with increasing concentrations of NPs (0.0, 6.25, 12.50, 25.00, 50.00, and 100.0 ppm). At the end of the incubation, cultures were washed with Dulbecco's phosphate-buffered saline (DPBS, Gibco) and the medium was replaced with 100 μL of ultrapure water. Four freeze/thaw cycles (from −80 to 37 °C) were performed to allow cell lysis and dsDNA release. The dsDNA quantification was carried out in Corning Costar 96-well black polystyrene plates following the manufacturer's instructions. Fluorescence levels were detected using a Victor X3 multilabel plate reader (λ_{ex} 360 and λ_{em} 460 nm) and correlated to the dsDNA content and thus to the cell number.

Further information on the cytotoxicity effect of the NPs was achieved by performing the LIVE/DEAD cell viability assay (Thermo Fisher) according to the manufacturer's instructions. Cells were seeded in μ-Plate 96-Well Black (Ibidi) at 10 000 cells per cm^2 and incubated overnight. Thereafter, the cells were treated for 72 h with increasing concentrations of NPs (0.0, 6.25, 12.50, 25.00, 50.00, and 100.0 ppm). After the treatment, cultures were rinsed with DPBS and incubated for 20 min with fresh medium containing 5 μg mL^{-1} Hoechst, 4 μM ethidium homodimer-1 (Thermo Fisher), and 2 μM calcein-AM (Thermo Fisher). Imaging was performed using a fluorescence microscope (Eclipse Ti, Nikon) equipped with a 10× objective. The acquired images were subjected to analysis using ImageJ, where the relative quantities of dead cells (ethidium homodimer-1-positive cells) and viable cells (calcein-positive cells) were counted within each specific condition.

Inductively coupled plasma mass spectrometry (ICP-MS) was used to evaluate the cellular uptake of the NPs. Cells were seeded at 10 000 cells per cm^2 density and incubated overnight; thereafter, half of the samples were treated for 72 h with a 100 ppm NPs concentration. Then the cells were detached and counted to determine their number and subsequently resuspended in DPBS for the following ICP-MS analysis.

Characterization and performance evaluation of the chitosan formulation

We compared the morphology of the formulations through scanning electron microscopy (SEM) analysis using a JEOL JSM-6490LA microscope with a thermionic source (W filament).

The viscosity of the formulations was determined to choose the best application method. Rheology analyses were performed by using a Modular Compact Rheometer (MCR 102) from Anton Paar GmbH with a No. 3912 coaxial cylinder measuring system. 5 mL of each formulation were poured in a cylindrical cup (radius of 14.452 mm) using a measuring bob with a radius of 13.331 mm, a ratio of radii of 1.084, and a gap length of 39.998 mm. Each measurement was performed with a cone angle of 120° and a measuring gap of 1.121 mm. RheoCompass software was used to collect data, which were then processed using OriginPro 2022 software (OriginLab Corporation, Northampton, MA, USA).

After applying the formulation to the mock-ups, the coating was studied in terms of morphology, color variation, surface water contact angle, protecting ability, and water vapor permeability.

Morphological analyses were performed by collecting images of the mock-ups before and after the application of the coating using a NYKON stereomicroscope model SMZ 745T (European Headquarters Nikon Europe BV, Tripolis 100, Burgerweeshuispad 101, 1076 ER Amsterdam, the Netherlands). Additionally, the color variation produced by the application of the coating was monitored using a Konica Minolta CM 700d spectrophotometer with an 8-degree viewing angle geometry, a diffusion light xenon lamp, and a high-resolution monolithic polychromator. A circular area with a diameter of 8 mm was tested for each measurement, and the results were obtained as the average of three different measures carried out on different mock-ups treated with the same coating formulation. Measurements were performed in the CIELAB1976 space and elaboration was carried out using SpectraMagic NX software. The color variation is defined in terms of ΔE, which was calculated as follows:[92]

$$\Delta E = \sqrt{\Delta L^2 + \Delta a^2 + \Delta b^2}$$

where ΔL, Δa, and Δb are the differences between the values obtained before and after the application of the coating on each sample. The parameters represent luminosity, red-green, and blue-yellow, respectively.

The surface contact angle was measured using an FTA 1000 analyzer system (First Ten Angstroms Inc., Newark, CA, USA) by dropping a 10 μL drop of water on the surface and instantaneously acquiring an image of this drop. The measurements were performed on three different points of the surface of each mock-up. The contact angle was then determined by analyzing each image using the software ImageJ and averaging the obtained contact angles for each formulation.

The protective ability of the coating and the water vapor permeability were determined by following the norms UNI 10921:2001[93] and UNI 15803:2010,[94] respectively.

Fresco mock-ups ageing and coating performance assessment

CeO_2 NPs were added to the cs04 and cs1 formulations to achieve a final concentration of 25 ppm. The addition was performed at room temperature while stirring at 800 rpm during the preparation of the formulation. The coating formulations were applied to the surface of simplified mock-ups as previously described (brush painting; 0.125 mL cm^{-2}). In order to test the efficacy of the CeO_2 NP-based coatings, the coated mock-ups and an uncoated sample were subjected to an accelerated ageing protocol, as described in a previous study.[83] First, they were placed in closed plastic Petri dishes containing a 0.1 M NaCl solution at 27.0 °C, making sure that only the bottom part of the sample came into contact with the solution itself. This allows the reproduction of the interaction with chlorine-based salts through capillary absorption from the bottom of the structure. The exposure to the NaCl solution was performed in the dark for 12 hours. Then, while the samples were still wet, they were placed in a Q-Sun Xe-1S climatic chamber (Q-LAB Corporation, Westlake, OH 44145-1419 SUA) and they were exposed to 8-hour cycles of UV light (65 W m^{-2}) at 50 °C, up to 72 hours of total exposure. Exposure to UV light under wet conditions simulates a highly humid environment.

Two archaeological fresco fragments were also exposed to this same degradation protocol, up to 72 hours of UV exposure. One of these samples was preemptively coated with the cs1-NPs formulation, while the other was considered as a reference of normal degradation. Visible aesthetic variations were monitored by acquiring photographs of the fragments before and after the degradation.

Between each repetition, the mock-ups were tested in terms of morphological and color variation, as described in the study of the chitosan coating in the previous section. Each acquisition was performed on two distinct points of the surface of each mock-up to account for heterogeneity and the colorimetric measurements were performed as an average of three measurements on each spot. After the completion of the tests, Raman spectra were acquired on different spots of the uncoated sample to determine the chemical composition of the degraded and non-degraded portions. A DXRTM3 Raman microscope with a 532 nm laser source was used to acquire the spectra. The conditions of each measurement were kept constant to better compare the results from different areas. The laser power level was set to 1.0 mW with a grating of 900 lines mm^{-1}. A 10× microscope objective was used, and a 25 μm pinhole aperture was set. Each measurement was performed after 2 exposures of 60 seconds, with a resolution of 1.9285 Raman shift (cm^{-1}). After the surface characterization, a portion of the pictorial layer was removed from the uncoated samples, and the powder was characterized through XPS. This last characterization was performed using a Kratos Axis Ultra DLD spectrometer (Kratos Analytical Ltd) with a monochromatic Al Kα X-ray source ($h\nu$ = 1486.6 eV) operating at 20 mA and 15 kV. Each specimen, in powder form, was prepared by pressing about 500 mg of powder onto a conductive indium substrate to obtain a film as much flat as possible. The wide scans were obtained over an analysis area of 300 × 700 μm^2 at a photoelectron pass energy of 160 eV and an energy step of 1 eV, while high-resolution spectra of Hg 4f and S 2p were obtained at a photoelectron pass energy of 20 eV and an energy step of 0.1 eV. A take-off angle of 0° with respect to the sample normal direction was used for all analyses. The differential electrical charging effects observed on all samples were neutralized. The spectra were referenced to the adventitious carbon 1s peak at 284.8 eV. The spectra were analyzed using CasaXPS software (Casa Software Ltd, version 2.3.25)[95] and the residual background was eliminated using the Shirley method across the binding energy range of the peaks of interest.

Author contributions

Conceptualization: E. G., G. C., F. M., A. T., and M. M.; methodology: E. G., S. M., S. D., R. B., M. G. R., F. M., and M. M.; investigation: E. G., S. M., S. D., R. B., A. C., M. B., and M. M.; visualization: E. G., S. M., S. D., R. B., A. C., M. B., and M. M.; supervision: G. C., F. M., A. T., and M. M.; writing – original draft: E. G., F. M., A. T., and M. M.; writing – review & editing: E. G., S. M., S. D., R. B., A. C., R. L., F. M., A. T., and M. M.

Conflicts of interest

There are no conflicts to declare.

Data availability

All data collected within this research are reported in the main text of the article and in its supplementary information (SI). Supplementary information includes additional data on the characterization of the nanoparticles and the coating, and additional information on the case study described. See DOI: https://doi.org/10.1039/d5nr02680f.

Acknowledgements

The authors acknowledge the CERIC-ERIC Consortium for the access to experimental facilities and financial support. We are grateful to Federico Catalano, Tania Fantinel, and Filippo Drago for performing SEM and ICP-MS analyses. We also thank Francesco De Boni who performed XPS characterization and Tomáš Hrbek for his help with environmental XPS measurements.

The fresco fragments shown in this article are identified with the Italian National ID 586026 and have been generously provided by the Museo archeologico nazionale di Aquileia – Italia. Images in Fig. 6 are used on the authorisation of the Ministero della cultura, Museo Storico e Parco del Castello di Miramare – Direzione regionale Musei nazionali Friuli Venezia Giulia. The use of these images is regulated by the current legislation (art. 108, co. 3 del D. Lgs 42/2004 s.m.i. – DM 161/23 – DM 108/24). Any reproduction, duplication or manipulation is strictly prohibited. The authors gratefully acknowledge the Parco Archeologico di Pompei, Italy, for generously granting permission to reproduce the fresco image shown in the graphical abstract.

References

1 G. Xiao, H. Li, Y. Zhao, H. Wei, J. Li and H. Su, *ACS Appl. Nano Mater.*, 2022, **5**, 14147–14170.

2 K. Reed, A. Cormack, A. Kulkarni, M. Mayton, D. Sayle, F. Klaessig and B. Stadler, *Environ. Sci.: Nano*, 2014, **1**, 390–405.

3 F. Caputo, M. D. Nicola, A. Sienkiewicz, A. Giovanetti, I. Bejarano, S. Licoccia, E. Traversa and L. Ghibelli, *Nanoscale*, 2015, **7**, 15643–15656.

4 Y. Li, X. Hou, C. Yang, Y. Pang, X. Li, G. Jiang and Y. Liu, *Sci. Rep.*, 2019, **9**, 2595.

5 R. Huang, X. Du, H. Wang, X. Cheng and Z. Du, *J. Appl. Polym. Sci.*, 2022, **139**, 51927.

6 R. Álvarez-Asencio, R. W. Corkery and A. Ahniyaz, *RSC Adv.*, 2020, **10**, 14818–14825.

7 S. Yasmeen, M. R. Khan, K. Park, Y. Cho, J. W. Choi, H.-S. Moon and H.-B.-R. Lee, *Ceram. Int.*, 2020, **46**, 12209–12215.

8 S. V. Harb, A. Trentin, T. A. C. de Souza, M. Magnani, S. H. Pulcinelli, C. V. Santilli and P. Hammer, *Chem. Eng. J.*, 2020, **383**, 123219.

9 K. An, Y. Sui, Y. Qing, C. Yang, C. Long, L. Wang and C. Liu, *Colloids Surf., A*, 2021, **625**, 126904.

10 B. Fotovvat, M. Behzadnasab, S. M. Mirabedini and H. E. Mohammadloo, *Colloids Surf., A*, 2022, **648**, 129157.

11 A. Joseph, K. P. John Mathew and S. Vandana, *ACS Appl. Nano Mater.*, 2021, **4**, 834–849.

12 I. Martín-Fabiani, M. L. Koh, F. Dalmas, K. L. Elidottir, S. J. Hinder, I. Jurewicz, M. Lansalot, E. Bourgeat-Lami and J. L. Keddie, *ACS Appl. Nano Mater.*, 2018, **1**, 3956–3968.

13 K. An, Y. Wang, Y. Sui, Y. Qing, W. Tong, X. Wang and C. Liu, *J. Rare Earths*, 2025, **43**(2), 227–245.

14 L. G. Ecco, M. Fedel, A. Ahniyaz and F. Deflorian, *Prog. Org. Coat.*, 2014, **77**, 2031–2038.

15 S. Fu, Z. Sun, P. Huang, Y. Li and N. Hu, *Nano Mater. Sci.*, 2019, **1**, 2–30.

16 J. Janesch, I. Czabany, C. Hansmann, A. Mautner, T. Rosenau and W. Gindl-Altmutter, *Prog. Org. Coat.*, 2020, **138**, 105409.

17 N. Karak, in *Nanomaterials and Polymer Nanocomposites*, ed. N. Karak, Elsevier, 2019, pp. 1–45.

18 K. Zarschler, L. Rocks, N. Licciardello, L. Boselli, E. Polo, K. P. Garcia, L. De Cola, H. Stephan and K. A. Dawson, *Nanomedicine*, 2016, **12**, 1663–1701.

19 B. H. Kim, M. J. Hackett, J. Park and T. Hyeon, *Chem. Mater.*, 2014, **26**, 59–71.

20 E. Spielman-Sun, E. Lombi, E. Donner, D. Howard, J. M. Unrine and G. V. Lowry, *Environ. Sci. Technol.*, 2017, **51**, 7361–7368.

21 C. K. Kim, T. Kim, I.-Y. Choi, M. Soh, D. Kim, Y.-J. Kim, H. Jang, H.-S. Yang, J. Y. Kim, H.-K. Park, S. P. Park, S. Park, T. Yu, B.-W. Yoon, S.-H. Lee and T. Hyeon, *Angew. Chem., Int. Ed.*, 2012, **51**, 11039–11043.

22 T. V. Plakhova, A. Y. Romanchuk, S. M. Butorin, A. D. Konyukhova, A. V. Egorov, A. A. Shiryaev, A. E. Baranchikov, P. V. Dorovatovskii, T. Huthwelker, E. Gerber, S. Bauters, M. M. Sozarukova, A. C. Scheinost, V. K. Ivanov, S. N. Kalmykov and K. O. Kvashnina, *Nanoscale*, 2019, **11**, 18142–18149.

23 A. L. Popov, N. R. Popova, N. V. Tarakina, O. S. Ivanova, A. M. Ermakov, V. K. Ivanov and G. B. Sukhorukov, *ACS Biomater. Sci. Eng.*, 2018, **4**, 2453–2462.

24 A. L. Popov, N. Popova, D. J. Gould, A. B. Shcherbakov, G. B. Sukhorukov and V. K. Ivanov, *ACS Appl. Mater. Interfaces*, 2018, **10**, 14367–14377.

25 A. L. Popov, N. R. Popova, I. I. Selezneva, A. Y. Akkizov and V. K. Ivanov, *Mater. Sci. Eng., C*, 2016, **68**, 406–413.

26 R. Mehmood, N. Ariotti, J. L. Yang, P. Koshy and C. C. Sorrell, *ACS Biomater. Sci. Eng.*, 2018, **4**, 1064–1072.

27 E. Grulke, K. Reed, M. Beck, X. Huang, A. Cormack and S. Seal, *Environ. Sci.: Nano*, 2014, **1**, 429–444.

28 S. Seal, A. Jeyaranjan, C. J. Neal, U. Kumar, T. S. Sakthivel and D. C. Sayle, *Nanoscale*, 2020, **12**, 6879–6899.

29 M. Maguregui, U. Knuutinen, K. Castro and J. M. Madariaga, *J. Raman Spectrosc.*, 2010, **41**, 1400–1409.

30 M. Cotte, J. Susini, N. Metrich, A. Moscato, C. Gratziu, A. Bertagnini and M. Pagano, *Anal. Chem.*, 2006, **78**, 7484–7492.

31 M. Radepont, W. de Nolf, K. Janssens, G. V. der Snickt, Y. Coquinot, L. Klaassen and M. Cotte, *J. Anal. At. Spectrom.*, 2011, **26**, 959–968.

32 F. Da Pieve, C. Hogan, D. Lamoen, J. Verbeeck, F. Vanmeert, M. Radepont, M. Cotte, K. Janssens, X. Gonze and G. Van Tendeloo, *Phys. Rev. Lett.*, 2013, **111**, 208302.

33 M. Salvadori and C. Sbrolli, *Archaeol. Anthropol. Sci.*, 2021, **13**, 187.

34 D. Jiménez-Desmond, J. S. Pozo-Antonio and A. Arizzi, *J. Cult. Herit.*, 2024, **66**, 166–186.

35 P. Fermo, G. Cappelletti, N. Cozzi, G. Padeletti, S. Kaciulis, M. Brucale and M. Merlini, *Appl. Phys. A*, 2014, **116**, 341–348.

36 J. Brus and P. Kotlík, *Stud. Conserv.*, 1996, **41**, 109–119.

37 A. Tsakalof, P. Manoudis, I. Karapanagiotis, I. Chryssoulakis and C. Panayiotou, *J. Cult. Herit.*, 2007, **8**, 69–72.

38 S. A. Ruffolo and M. F. La Russa, *Front. Mater.*, 2019, **6**, 147.

39 M. Zucchelli, G. Mazzon, L. Bertolacci, R. Carzino, E. Zendri and A. Athanassiou, *Prog. Org. Coat.*, 2021, **159**, 106434.

40 S. Andreotti, E. Franzoni, M. Degli Esposti and P. Fabbri, *Materials*, 2018, **11**, 165.

41 S. Mandal, P. Kumar, B. Satpathy, K. Das and S. Das, *J. Cult. Herit.*, 2024, **69**, 94–112.

42 D. Colangiuli, M. Lettieri, M. Masieri and A. Calia, *Sci. Total Environ.*, 2019, **650**, 2919–2930.

43 P. M. Carmona-Quiroga, S. Martínez-Ramírez and H. A. Viles, *Appl. Surf. Sci.*, 2018, **433**, 312–320.

44 M. F. La Russa, N. Rovella, M. Alvarez de Buergo, C. M. Belfiore, A. Pezzino, G. M. Crisci and S. A. Ruffolo, *Prog. Org. Coat.*, 2016, **91**, 1–8.

45 P. Munafò, G. B. Goffredo and E. Quagliarini, *Constr. Build. Mater.*, 2015, **84**, 201–218.

46 L. O. Cinteză, M. A. Tănase, L. O. Cinteză and M. A. Tănase, in *Thin Films*, IntechOpen, 2020.

47 S. A. Ruffolo, M. F. La Russa, M. Malagodi, C. Oliviero Rossi, A. M. Palermo and G. M. Crisci, *Appl. Phys. A*, 2010, **100**, 829–834.

48 S. A. Ruffolo, M. F. La Russa, P. Aloise, C. M. Belfiore, A. Macchia, A. Pezzino and G. M. Crisci, *Appl. Phys. A*, 2014, **114**, 753–758.

49 J. Otero, V. Starinieri, A. E. Charola and G. Taglieri, *Constr. Build. Mater.*, 2020, **230**, 117112.

50 J. Otero, V. Starinieri and A. E. Charola, *Constr. Build. Mater.*, 2018, **181**, 394–407.

51 M. J. Mosquera, L. A. M. Carrascosa and N. Badreldin, *Pure Appl. Chem.*, 2018, **90**, 551–561.

52 A. Chatzigrigoriou, P. N. Manoudis and I. Karapanagiotis, *Macromol. Symp.*, 2013, **331–332**, 158–165.

53 L. de Ferri, P. P. Lottici, A. Lorenzi, A. Montenero and E. Salvioli-Mariani, *J. Cult. Herit.*, 2011, **12**, 356–363.

54 I. Franco-Castillo, L. Hierro, J. M. de la Fuente, A. Seral-Ascaso and S. G. Mitchell, *Chem*, 2021, **7**, 629–669.

55 M. R. Caruso, G. D'Agostino, S. Milioto, G. Cavallaro and G. Lazzara, *J. Mater. Sci.*, 2023, **58**, 12954–12975.

56 R. Lamuraglia, A. Campostrini, E. Ghedini, A. De Lorenzi Pezzolo, A. Di Michele, G. Franceschin, F. Menegazzo, M. Signoretto and A. Traviglia, *Coatings*, 2023, **13**, 277.

57 A. Badia, A. Duarri, A. Salas, J. Rosell, J. Ramis, M. F. Gusta, E. Casals, M. A. Zapata, V. Puntes and J. García-Arumí, *ACS Nano*, 2023, **17**, 910–926.

58 M. Kurian and C. Kunjachan, *Int. Nano Lett.*, 2014, **4**, 73–80.

59 R. K. Hailstone, A. G. DiFrancesco, J. G. Leong, T. D. Allston and K. J. Reed, *J. Phys. Chem. C*, 2009, **113**, 15155–15159.

60 E. G. Heckert, A. S. Karakoti, S. Seal and W. T. Self, *Biomaterials*, 2008, **29**, 2705–2709.

61 W.-J. Jeon, H. Kim and S.-H. Byeon, *Colloids Surf., A*, 2022, **640**, 128416.

62 T. Skála, F. Šutara, K. C. Prince and V. Matolín, *J. Electron Spectrosc. Relat. Phenom.*, 2009, **169**, 20–25.

63 E. Bêche, P. Charvin, D. Perarnau, S. Abanades and G. Flamant, *Surf. Interface Anal.*, 2008, **40**, 264–267.

64 A. Murali, Y.-P. Lan and H. Y. Sohn, *Nano-Struct. Nano-Objects*, 2019, **18**, 100257.

65 Y. Ma, W. Gao, Z. Zhang, S. Zhang, Z. Tian, Y. Liu, J. C. Ho and Y. Qu, *Surf. Sci. Rep.*, 2018, **73**, 1–36.

66 J. Henych, M. Šťastný, J. Ederer, Z. Němečková, A. Pogorzelska, J. Tolasz, M. Kormunda, P. Ryšánek, B. Bażanów, D. Stygar, K. Mazanec and P. Janoš, *Environ. Sci.: Nano*, 2022, **9**, 3485–3501.

67 R. Priyadarshi and J.-W. Rhim, *Innovative Food Sci. Emerging Technol.*, 2020, **62**, 102346.

68 L. Qi, S. Pal, P. Dutta, M. Seehra and M. Pei, *J. Biomed. Mater. Res., Part A*, 2008, **87A**, 236–244.

69 G. Thandapani, P. Supriya Prasad and P. N. Sudha, *Int. J. Biol. Macromol.*, 2017, **104**, 1794–1806.

70 Chitosan implants in the rat spinal cord: Biocompatibility and biodegradation - Kim - 2011 - Journal of Biomedical Materials Research Part A - Wiley Online Library, https://

onlinelibrary.wiley.com/doi/full/10.1002/jbm.a.33070?casa_token=rplEWb5TiQAAAAAA%3AK_YzXK64dy-kDMRZtgwZSw0XbVv3wJMtKBnnN8k_ihaFK-h1Q5OdTgJRMub-snQ9iQ9Dyi8dw7E5, (accessed September 1, 2025).

71 K. A. Dawson and Y. Yan, *Nat. Nanotechnol.*, 2021, **16**, 229–242.

72 G. G. Genchi, A. Degl'Innocenti, C. Martinelli, M. Battaglini, D. De Pasquale, M. Prato, S. Marras, G. Pugliese, F. Drago, A. Mariani, M. Balsamo, V. Zolesi and G. Ciofani, *ACS Appl. Mater. Interfaces*, 2021, **13**, 40200–40213.

73 G. G. Genchi, V. Mollo, M. Battaglini, M. Belenli Gümüş, A. Marino, M. Prato, S. Marras, F. Drago, G. Pugliese, F. Santoro and G. Ciofani, *ACS Appl. Nano Mater.*, 2023, **6**, 10853–10862.

74 M. Epple, V. M. Rotello and K. Dawson, *Acc. Chem. Res.*, 2023, **56**, 3369–3378.

75 S. D. Purohit, R. Priyadarshi, R. Bhaskar and S. S. Han, *Food Hydrocolloids*, 2023, **143**, 108910.

76 P. K. Panda, P. Dash, J.-M. Yang and Y.-H. Chang, *Cellulose*, 2022, **29**, 2399–2411.

77 Z. Kalaycıoğlu, N. Kahya, V. Adımcılar, H. Kaygusuz, E. Torlak, G. Akın-Evingür and F. B. Erim, *Eur. Polym. J.*, 2020, **133**, 109777.

78 P. N. Manoudis, I. Karapanagiotis, A. Tsakalof, I. Zuburtikudis, B. Kolinkeová and C. Panayiotou, *Appl. Phys. A*, 2009, **97**, 351–360.

79 C. Esposito Corcione, N. De Simone, M. L. Santarelli and M. Frigione, *Prog. Org. Coat.*, 2017, **103**, 193–203.

80 C. Oleari, *Standard Colorimetry: Definitions, Algorithms and Software*, John Wiley & Sons, 2015.

81 J. K. McCormack, *Miner. Deposita*, 2000, **35**, 796–798.

82 S. Pérez-Diez, A. Pitarch Martí, A. Giakoumaki, N. Prieto-Taboada, S. Fdez-Ortiz de Vallejuelo, A. Martellone, B. De Nigris, M. Osanna, J. M. Madariaga and M. Maguregui, *Anal. Chem.*, 2021, **93**, 15870–15877.

83 M. K. Neiman, M. Balonis and I. Kakoulli, *Appl. Phys. A*, 2015, **121**, 915–938.

84 R. Nöller, *Stud. Conserv.*, 2015, **60**, 79–87.

85 E. Gliozzo, *Archaeol. Anthropol. Sci.*, 2021, **13**, 210.

86 W. Anaf, K. Janssens and K. De Wael, *Angew. Chem.*, 2013, **125**, 12800–12803.

87 K. Keune and J. J. Boon, *Anal. Chem.*, 2005, **77**, 4742–4750.

88 M. Radepont, Y. Coquinot, K. Janssens, J.-J. Ezrati, W. de Nolf and M. Cotte, *J. Anal. At. Spectrom.*, 2015, **30**, 599–612.

89 K. Elert, M. Pérez Mendoza and C. Cardell, *Commun. Chem.*, 2021, **4**, 1–10.

90 J. Yu, W. S. Warren and M. C. Fischer, *Sci. Adv.*, 2019, **5**, eaaw3136.

91 T. Hrbek, P. Kúš, M. G. Rodríguez, V. Matolín and I. Matolínová, *Int. J. Hydrogen Energy*, 2024, **57**, 187–197.

92 G. Wyszecki and W. S. Stiles, *Color Science: Concepts and Methods, Quantitative Data and Formulas*, Wiley, 1967.

93 UNI 10921:2001 - UNI Ente Italiano di Normazione, https://store.uni.com/uni-10921-2001, (accessed October 16, 2024).

94 UNI EN 15803:2010 - UNI Ente Italiano di Normazione, https://store.uni.com/uni-en-15803-2010, (accessed October 16, 2024).

95 N. Fairley, V. Fernandez, M. Richard-Plouet, C. Guillot-Deudon, J. Walton, E. Smith, D. Flahaut, M. Greiner, M. Biesinger, S. Tougaard, D. Morgan and J. Baltrusaitis, *Appl. Surf. Sci. Adv.*, 2021, **5**, 100112.